Thermomechanical Deformation Behaviour of DH36 Steel during Friction Stir Welding by Experimental Validation and Modelling

Athanasios I. Toumpis[*1], Alexander M. Galloway[1], Larbi Arbaoui[2], Nicolas Poletz[2]

[1]Department of Mechanical & Aerospace Engineering, University of Strathclyde, Glasgow, UK

[2]Morfeo Team, Cenaero, Gosselies, Belgium

*Corresponding author, e-mail athanasios.toumpis@strath.ac.uk

Abstract

Friction stir welding is a solid state thermo-mechanical deformation process from which the plasticisation behaviour of the stirred material can be evaluated through the study of flow stress evolution. Flow stress data also supporting the development of a local microstructural numerical model have been generated. Hot compression testing of DH36 steel has been performed at a temperature range of 700^{o}C–1100^{o}C and strain rates from 10^{-3} s^{-1} to 10^{2} s^{-1} to study the alloy's thermo-mechanical deformation behaviour in conditions which simulate the actual friction stir welding process. It has been found that the evolution of flow stress is significantly affected by the test temperature and deformation rate. The material's constitutive equation and constants have been calculated after analysis of these data. Preliminary numerical analysis results are in good agreement with experimental observations.

Keywords: Friction stir welding; Thermo-mechanical deformation; Flow stress; Low alloy steel; Simulation; Modelling.

1. Introduction

Friction stir welding (FSW) is a solid state joining process during which the material is thermo-mechanically worked by a specially designed rotating non-consumable tool.[1] The material is heated to a high enough temperature for plastic deformation to occur[2] but below the solidus.[3] FSW is a very complex process incorporating mechanical and thermal processing of the material, considerable plastic deformation and high levels of flow stress;[4] as no melting of the material takes place, it is a process analogous to forging[5,6] rather than casting which more closely resembles the conditions observed during conventional fusion welding. FSW is currently being extensively employed in aluminium joining applications[7] but there is significant interest by many industrial sectors in transferring the process and its advantages to steel. Previous publications on the application of FSW to steel report that there are several positive effects on the properties such as considerable grain refinement,[8] overmatching of the parent metal,[9] minimised distortion,[10] and potential for welding speeds which can be competitive to fusion welding methods.[11]

The behaviour of a metal under thermo-mechanical deformation, as in the case of FSW, can be accurately represented by determining the evolution of flow stress as a function of test temperature and strain rate.[12] The flow stress of a material, the stress that yields the material as a function of strain, is an important consideration when deciding on the basic parameters of a metalworking process.[13-15] It is influenced by many factors; material properties such as grain size, crystal structure, existing phases, and process requirements including temperature and strain rate.[12,14] FSW is developed by thermo-mechanical stirring hence can be viewed as one such metalworking process. Therefore, it is critical that an understanding of the flow stress generated over a range of temperatures and strain rates is achieved such that improvements in the accuracy of any predictive modelling being undertaken will be more robust as a result of these experimental data. Clearly, the experimental conditions to be adopted, i.e. test temperature and rate of deformation need to closely match the actual conditions occurring during FSW.

This study reports on the development of a local microstructural numerical model which takes into consideration the deformation of the metal by the stirring action of the pin of the FSW tool, and only a few millimetres around this pin that has been plunged in between the two plates to be welded. Modelling of FSW is a highly complicated task since the physical mechanisms occurring during the process are not fully understood, and in particular those concerning the heat generation within the weld joint. Some models introduced in the relevant literature neglect the intense material flow and assume purely sliding frictional contact. By fitting their experimental thermal cycles, Zahedul *et al.*[16] obtain a rather low value for the friction coefficient, leading the researchers to conclude that a purely frictional heating model is probably not adequate. Simar *et al.*[17] observe that the tool's high maximum temperature, above the melting point of the aluminium alloy 6005A, predicted by assuming a

purely frictional contact confirms the need to allow for the material flow and the volume heat generation due to plastic deformation as part of the modelling effort.

The modelling work discussed herein aims to predict material flow, temperature distribution, phase change and heat generation associated with the FSW of DH36 steel, and concentrates on the thermo-mechanical effects during welding. A local thermo-fluid finite element model based on velocity/pressure formulation[18] is implemented to simulate the velocity and temperature distributions around the FSW tool. Plastic deformation and frictional heat generation are considered in the numerical model. Moreover, the results of this model are expected to provide the input data for microstructural evolution computations. The thermo-fluid model assumes a highly viscous non-Newtonian material behaviour. Due to the high temperature and strain rate conditions that prevail under the shoulder and around the pin of the tool during FSW, only the plastic deformation is taken into account as the extent of elastic deformation region is considered negligible in comparison. As a consequence, it is necessary to determine the evolution of viscosity, a property highly dependent on the material, with respect to temperature and strain rate. Therefore, establishing the actual flow stress of the material by hot compression testing will generate reliable validation data to support this local microstructural numerical model.

There are diverse thermo-mechanical deformation data on steels[15,19-27] and other alloys[28-31] available in the relevant technical literature, none of which is on steel grade DH36 and in conditions that simulate FSW. One publication[15] discusses the effect of temperature and strain rate on the high temperature ($850^{o}C$ – $1150^{o}C$) deformation behaviour of 42CrMo medium carbon low alloy steel by hot compression testing on a Gleeble thermo-mechanical simulator. It is reported that in high temperature and low strain rate deformation conditions, flow stress curves consist of four diverse stages which are governed by two opposing phenomena, work hardening and thermally induced softening, specifically dynamic recrystallisation (DRX) and dynamic recovery (DRV).[15] In conditions of lower temperature and higher strain rate however, the last two stages, i.e. the rapid decrease of flow stress due to DRX and high dislocation annihilation followed by a steady state flow stress are less discrete as DRV becomes the principal phenomenon. The same work[15] notes that the alloy's flow stress is greatly influenced by test temperature and strain rate. Deformation by hot compression occurs primarily by thermally induced phenomena, mainly DRX which is dependent on temperature and process duration; that is, increased temperature and decreased strain rate, i.e. deformation duration, offer more time for thermal energy accretion hence induce higher mobility at grain boundaries for DRX and dislocation annihilation to develop, both of which effectively decrease the flow stress. As explained,[15] flow softening is frequently exhibited by steel alloys in such thermo-mechanical deformation conditions associated with common metalworking processes.

Abbasi and Momeni[20] assess the hot workability of Fe-29Ni-17Co, the properties of which are highly affected in high temperature deformation processes, by hot

compression tests in the temperature range of 900°C–1200°C and strain rates from 10^{-3} s^{-1} to 10 s^{-1}, and a rather limited microstructural examination of the deformed samples. Discussing the flow stress curves of the alloy, they[20] note that DRX with a single peak is exhibited in the high temperature – low strain rate conditions, i.e. a grain refinement method. In low temperature – high strain rate testing conditions, the flow stress curves demonstrate a steady rise, without one distinctive peak, to the end of the deformation. In comparable terms to the above explanation,[15] the latter indicates that the extent of DRX is reduced because these conditions do not bear enough thermal activation energy; work hardening is the leading process in this case.[20] The metal's processing map, a map for identifying the processing conditions where the desirable effects of DRX occur, is also developed; the study[20] concludes that the processing map, mechanical testing and microstructural examination confirm that the most appropriate temperature range for hot deformation of the specific alloy is 1000°C – 1200°C due to its improved workability because of enhanced DRX.

Another study[24] is conducted in similar testing conditions, hot compression tests at 850°C–1150°C in strain rates of 10^{-4} s^{-1} to 3 s^{-1}, to evaluate the flow stress and the effect of DRX on the deformation behaviour of a medium carbon microalloyed steel. The presented analysis[24] is in agreement with the observations of the previous study;[20] nearly all flow stress curves for high test temperatures reveal a single peak stress and subsequent progressive decrease to a steady state stress hence the occurrence of DRX. Again, the single peak stress is difficult to identify with increasing strain rate or decreasing test temperature thus the impact of DRX is limited while at the lowest examined test temperature (850°C), no DRX but DRV takes place.[24]

In the case of the present thermo-mechanical deformation study, hot axisymmetric compression testing is undertaken in order to assess the behaviour of DH36 steel at elevated temperatures, and generate flow stress data reproducing the deformation which is developed during the actual FSW process. The intention is to validate the modelling work on FSW, improve the fundamental understanding of the process, assist in establishing process parameters and finally, improve the tooling and machine specifications during future FSW developments, e.g. pre-heat assisted FSW.

2. Experimental Procedure

Solid cylindrical specimens (diameter: 9 mm, length: 18 mm) were produced from a 10 mm thick rolled plate of steel grade DH36, a low alloy steel utilized in the European construction and shipbuilding industry, in the as received condition. The flow stress of the material was recorded for 25 diverse sets of temperature and medium to high strain rate (Table 1) by performing 58 uniaxial hot compression tests on a Gleeble 3800 thermo-mechanical testing system.

Table 1 Number of tests performed per set of test temperature and strain rate

Test parameters	10^{-3} s^{-1}	10^{-2} s^{-1}	10^{-1} s^{-1}	1 s^{-1}	10 s^{-1}	50 s^{-1}	10^{2} s^{-1}
700°C	3	2					
750°C	2	2	2				
800°C	2	3	3				
850°C		3	2	3			
900°C			2	2	3	2	
950°C				2	3	2	2
1000°C					3	2	2
1100°C					2	2	2

The deformation parameters of Table 1 and the thermal cycle of the simulation are based on an analysis of data generated by thermocouples that were accurately positioned in various regions within the weld zone of 6 mm DH36 plates subjected to FSW, as part of Project HILDA (deliverable D4.2) acknowledged by the authors. The temperature distribution map of Fig. 1 was produced by this study. In this analysis, material flow occurring below 700°C and with low strain rate is found to be essentially insignificant. Conversely, the metal under the shoulder and around the pin of the tool is found to be experiencing temperatures close or above 1000°C and high strain rates (10 s^{-1}–100 s^{-1}). These conditions are therefore the processing envelope of FSW and are appropriate for a simulation of the process.

The testing programme has been implemented according to the guidelines set by Roebuck *et al.*[32] The consistent experimental procedure which was followed throughout the testing programme is outlined below:

1. Spot welding thermocouples onto the sample,
2. Applying conductive paste and fixing small graphite plates on the two faces of the sample to prevent bonding of the steel samples with the anvils of the machine. Samples used at the very high test temperatures (above 1000°C), where graphite is expected to react with steel, were fitted with thin pieces of tantalum foil.
3. Inserting and securing the sample in the Gleeble (Fig. 2),
4. Heating each sample at a heating rate of 80°C s^{-1} using direct resistance heating,
5. Equalising the temperature for one minute in order to ensure that the compressive test occurs when the required test temperature is homogenous in the entire sample,
6. Performing the compressive test in vacuum, at the homogenous temperature (isothermal) and up to 0.693 strain (standard 50% deformation),
7. Ending compressive test and air cooling each sample at a predetermined cooling rate for each test temperature, in the range of 10 – 20°C s^{-1}.

3. Results and discussion

3.1. Flow stress analysis

Thermo-mechanical deformation data were generated for each set of conditions outlined in Table 1, and these data were plotted in stress strain charts to evaluate their consistency. Each plotted curve is the flow stress of DH36 parent material within specific boundary conditions (test temperature, strain rate and strain). Two tests were conducted for each set of conditions and in most cases, the consistency of the results was found to be very good or excellent (Fig. 3). Where the repeatability of the data was found inadequate due to minor deviations in the flow stress curves, a third test was performed. The temperature profile for each test was also plotted in order to provide confirmation that the required thermal cycle was followed and that the test temperature was kept constant during the equalising and deformation stages. One such plotted temperature profile is presented in Fig. 4. Further, the strain rate profile (strain rate vs. strain) was plotted for the deformation stage of each test to verify that the prescribed strain rate was exerted on the sample during the majority of the deformation (Fig. 5).

The evolution of the flow stress follows two patterns[12,14,15,20,24] and these were verified in DH36. First, the flow stress is seen to increase with increasing strain rate. This is represented in Fig. 6 where the flow stress curves of four tests with increasing strain rate and constant temperature have been superimposed. Second, the flow stress is seen to decrease with increasing temperature. This relation is exhibited in Fig. 7 where four tests of increasing temperature and constant strain rate of 10^{-2} s^{-1} have been plotted. Hence, the flow softening phenomenon is found to be more pronounced as strain rate is seen to decrease for a fixed temperature (Fig. 6), and as deformation temperature is seen to increase at a constant strain rate (Fig. 7). It has been confirmed by previous studies[15,20] that there is either more deformation time or higher temperature respectively for thermal energy build-up which promotes DRX. As a consequence, the flow stress is seen to increase but at a decreasing rate in both figures.

Two of the four flow stress curves in Fig. 6 (strain rate of 10^{-1} s^{-1} & 1 s^{-1}), i.e. low strain rates at a high temperature, and all curves of Fig. 7, i.e. flow stress at very low strain rate (10^{-2} s^{-1}) exhibit the common DRX behaviour with a relatively distinct single peak also reported by a previous study.[20] Thus, extensive grain refinement is expected to be occurring in such deformation conditions which simulate regions of a typical FSWeld. One peak stress becomes difficult to determine as the strain rate is seen to increase for the constant deformation temperature of 900^{o}C (Fig. 6), particularly for the tests in strain rate of 10 s^{-1} & 50 s^{-1}. This suggests that the influence of DRX is reduced similarly to what is discussed in another publication.[24] Table 2 presents the average value of the recorded flow stress for each set of deformation parameters that were tested, and for 0.3 strain. The values in the table

verify the previously mentioned effect of increasing temperature and strain rate on flow stress.

Table 2 Average flow stress (in MPa) for each set of parameters at 0.3 strain

	10^{-3} s^{-1}	**10^{-2}** s^{-1}	**10^{-1}** s^{-1}	**1** s^{-1}	**10** s^{-1}	**50** s^{-1}	**10^{2}** s^{-1}
700°C	109	163.5					
750°C	95	144	202				
800°C	103	156	204				
850°C		137	180	214			
900°C			154	190	236	257	
950°C				163	209.5	237	227
1000°C					188.5	215	205
1100°C					151	163	165

There are however three anomalous datasets in Table 2 (marked in the table), all at the same test temperature of 800°C (at 10^{-3} s^{-1}, 10^{-2} s^{-1} and 10^{-1} s^{-1}) which contradict the relation of increasing temperature/decreasing flow stress. In these three cases, the flow stress is higher than the one recorded for 750°C and constant strain rate (also visible in Fig. 7). This atypical behaviour of DH36 at 800°C has been established from 8 tests in total (Table 1) therefore would appear well validated. It can be argued that this irregularity is caused by an abrupt change in the deformation behaviour of DH36 steel due to its dual phase of ferrite and austenite at that temperature. Indeed, the test temperature of 800°C seems to be the only one examined which is well within the intercritical temperature range of steel.

Although beyond the scope of the current study, the exact cause of this atypical behaviour along with an evaluation of the effect of the thermal cycle and strain rate on the resultant microstructure will be examined further by metallographic preparation and microstructural characterisation of the deformed (in conditions simulating FSW) samples. It is worth noting here that the hot compression tests in the majority of similar deformation studies on steel alloys[15,20,24] are conducted above 850°C, therefore essentially above the A_3 temperature (almost fully austenitic microstructure), because these studies are concerned with establishing the flow stress in conditions appropriate for metalworking processes. Thus, this atypical behaviour of steel at 800°C has not been reported previously, to the best knowledge of the authors.

3.2. Flow stress constitutive equation and deformation constants

The flow stress data generated from this detailed thermo-mechanical study of DH36 were introduced in a 3D thermo-fluid model.[33] This model is developed to predict the temperature and material flow during FSW of DH36 steel.[34,35] It consists of stationary

staggered flow and thermal computation. The flow problem is solved using a mixed velocity/pressure analysis described using Eulerian instead of Lagrangian formulation to avoid high element distortions and time-consuming re-meshing operations.[36] The plastic work is calculated from the simulation of flow and is used as the heat source for the thermal calculation. The friction contribution to the heat generation is computed from the friction shear stress and the relative sliding velocity at the tool/plate interface.[37,38]

The numerical model is based on a flow formulation and the discretisation of the conservation of mass and momentum.[39] In terms of mass conservation, the density variation with space and time of the examined material is neglected. Hence, the material can be considered as incompressible. The mass conservation in a volume domain Ω is simplified to the following continuity equation[40]

$$\vec{\nabla} \cdot \vec{\upsilon} = 0 \qquad (1)$$

where $\vec{\upsilon}$ is the velocity field.

With regard to momentum conservation, it is known that the Reynolds number for fluids with high viscosity is very low (smaller than 1). For FSW of stainless steel as an example, the Reynolds number is approximately 5×10^{-6}.[41] The inertial term can be neglected compared to the viscous term for the modelling of the process.[42] The force of gravity is also assumed to be small in comparison to viscous stress. The momentum conservation equation is then simplified as

$$\vec{\nabla} \cdot \sigma = 0 \qquad (2)$$

where σ is the Cauchy stress tensor which can be expressed as a function of the deviatoric stress tensor s and the hydrostatic pressure p

$$\sigma = s - pI \qquad (3)$$

where I is the identity matrix.

The constitutive equation (4) predicts the behaviour of DH36 through the relation between stress and strain rate by considering the following assumptions. For a thermo-mechanical process such as FSW which involves very large deformation, the elastic strain can be neglected compared to plastic strain. A rigid visco-plastic approximation is employed herein,[43] and the deviatoric stress tensor is only express as a function of the strain rate tensor

$$s = 2\mu \dot{\varepsilon}_{vp} \qquad (4)$$

where $\dot{\varepsilon}_{vp}$ is the deviatoric strain rate tensor and μ is the effective viscosity. During FSW, the effective viscosity is varying due to the dynamic aspect of the process. A Norton-Hoff visco-plastic law has been used; in this law, the stress is expressed as a power function of the strain rate with two thermally dependent material parameters K and m

$$s = 2K(\sqrt{3}\,\dot{\varepsilon}_{vp}^{eq})^m\,\dot{\varepsilon}_{vp} \quad (5)$$

where *K* is the dynamic viscosity or consistency of the material and *m* the strain rate sensitivity coefficient. These two material parameters have been calculated on a range of temperatures based on the sets of conditions outlined in Table 1.

Stress values are extracted for several strain values from the flow stress data. For each temperature, a linear regression is performed between logarithmic values of stress and strain rate

$$\log(\sigma^{eq}) = A\log(\sqrt{3}\,\dot{\varepsilon}_{vp}^{eq}) + B \quad (6)$$

where *A* and *B* are coefficients of the linear regression; σ^{eq} is the equivalent stress, following the Von Mises criterion expressed as a function of equivalent strain rate $\dot{\varepsilon}_{vp}^{eq}$ as

$$\sigma^{eq} = \sqrt{\frac{2}{3}s:s} = \sqrt{3}K(\sqrt{3}\,\dot{\varepsilon}_{vp}^{eq})^m \quad (7)$$

For each temperature, the consistency and strain rate sensitivity are determined by

$$\begin{cases} K(T) = \dfrac{B(T)}{\sqrt{3}} \\ m(T) = A(T) \end{cases} \quad (8)$$

The material consistency and strain rate sensitivity are estimated at each temperature of the experimental plan as shown in Figs. 8 and 9 respectively. A tabulated Norton-Hoff law is obtained from this analysis for the 700°C–1100°C temperature range.

3.3. Model implementation

A 3D numerical analysis of material and thermal flow during FSW of DH36 was produced based on the identification of the alloy's visco-plastic behaviour. The finite element model is focused on a region located around the tool (Fig. 10).[44,45] The computational domain is composed of three main subdomains: the tool, the workpiece and the backing plate. The workpiece is represented by the middle disc centred on the tool. The two steel plates to be welded are described in a single domain composed of the same material, DH36. A standard pcBN-WRe FSW tool comprising a convex scrolled shoulder of diameter 25 mm, a convex threaded pin of base diameter 10 mm and length of 5.7 mm, and a WC shank was employed for the welding simulation; the model allows for the multi-material nature of this tool. The pitches on the pin and shoulder are not included in the mesh in order to obtain an axisymmetric, featureless shape. The pin of the tool is in the welding position (plunged in). All subdomains of the model are connected in a single mesh due to the Eulerian formulation. The fixation of the mesh induced by this executed Eulerian

formulation dictates that the FSW machine can only be modelled in position control; that is, the tool is positioned at a constant vertical distance from the workpiece irrespective of the forces acting upon the former. In addition, forces and torque are calculated as resulting from the mechanical computation.

The workpiece and backing plate are discs with radius of 80 mm, centred on the tool's rotational axis. The workpiece thickness is 6 mm and the backing plate thickness is 20 mm; the latter is treated as rigid and of typical steel thermal properties. The mesh has 203,761 nodes, and consists of 194,472 hexahedra and 29,736 wedges, i.e. 224,208 elements. The mesh is refined at the tool/workpiece interface and in the thermo-mechanically affected zone (TMAZ) in order to capture high temperature and velocity gradients in this region.

The strain rate sensitivity and consistency of the workpiece material are identified from the flow stress at 0.3 strain (Figs. 8 and 9). The consistency is seen to decrease from ~190 MPa s^m at 700°C to ~65 MPa s^m at 1100°C. The strain rate sensitivity in this temperature range varies between 0.1 and 0.18.

The boundary conditions applied in the thermo-fluid model are related to process parameters, i.e. tool traverse and rotational speed. The backing plate is subjected to a constant translational velocity which is the opposite of the tool traverse speed. The same velocity is imposed on the side of the workpiece to model the material inlet. To prevent outflow on free surfaces (e.g. workpiece top surface) or flow between parts (e.g. tool/workpiece interface), the normal velocity on these surfaces is constrained. The liquid cooling system on the tool holder is simulated with a condition of convection which is implemented on the side surfaces of the WC shank. Also, a friction condition is applied on the interface between tool and workpiece.[46] The tool velocity needed for the friction condition is an analytical field function of rotational velocity and is used to compute the sliding velocity (relative velocity between tool and welded material) on the interface.[47,48] The friction model is based on the Norton friction law, and is used to evaluate shear stress and power on this interface. The thermo-mechanical model is based on a weak coupling; the mechanical computation is coupled with the temperature through the thermo-mechanical behaviour law used for DH36. The thermal model is coupled with the flow model by heat advection which is a function of material flow, deformation heat flux generated by visco-plastic work and friction heat flux produced on the tool/workpiece interface. Two sets of process parameters are used in this analysis; 200 rpm tool rotational speed & 100 mm min^{-1} tool traverse speed, further identified as "cold" conditions, and 500 rpm-400 mm min^{-1} classified as "hot" conditions. The tool velocity is calculated on the tool/workpiece interface with a peak value of 0.147 m s^{-1} in the cold conditions and 0.366 m s^{-1} in the hot conditions, both reached at the shoulder external radius.

The temperature distribution results from numerical simulations with a partial tool penetration at a depth of 5.2 mm are presented for cold (Fig. 11*a*) and hot (Fig. 11*b*) conditions. The interface diameter is approx. 14 mm whilst the shoulder diameter is approx. 25 mm. In these simulations, the material is flowing from the advancing (right

side of Figs. 11, 12 and 13) to the retreating side (left side of same figures). The peak temperature is seen under the tool shoulder due to the heat generated by friction in addition to dissipated plastic deformation energy. This dissipation is induced by high strain rate in the material near the shoulder and pin as a result of the high tool rotational speed. The obtained temperatures in Fig. 11*a* are in the range of 650°C–1200°C, thus within the preliminary experimental results from thermocouple measurements (Fig. 1). A marginally elevated peak temperature of approx. 1250°C is found in the hot conditions (Fig. 11*b*), where lower diffusion of heat is also observed due to the higher traverse speed.

The TMAZ for the same tool penetration depth and for both conditions is displayed in Fig. 12; a composite image demonstrating the distribution of plastic strain (i.e. an accumulated plastic strain map) and shape of the TMAZ, and the heat affected zone (HAZ) temperature gradient is provided for the cold conditions (Fig.12*a*). The TMAZ for hot conditions is presented in Fig.12*b*, where the differently shaded particles in the centre correspond to the deformed region in the welded plate; that is, particles which have undergone plastic deformation.

The extent of the HAZ represented by the white lines (700°C isothermal line) of Fig. 11*a* and *b* is compared with experimental observations as shown in the macrograph of Fig. 13*a* for cold conditions and Fig. 13*b* for hot conditions. The outer lines define the HAZ of a DH36 steel FSWeld and the inner line delimits the TMAZ. The HAZ for both conditions computed by the local model corresponds to the same convex shape found experimentally. The simulated HAZ extension on the weld top surface of the cold conditions is 16.8 mm and of hot conditions is 14.6 mm. Both are comparable to the widths measured experimentally; 17 mm in Fig. 13*a* and 14.2 mm in Fig. 13*b*. On the macrographs' bottom surface, the HAZ width for cold and hot conditions is 9.2 mm and 2.2 mm respectively. The corresponding widths are numerically estimated as approx. 5.5 mm and 2.74 mm. This difference between experimental and numerical width of the HAZ bottom surface can be attributed to an overestimation of thermal energy exchange between the DH36 plates and the backing plate. The TMAZ is clearly asymmetric with respect to the tool axis in both conditions, i.e. wider on the retreating side compared to the advancing side. Its concave shape on the advancing side (Fig. 13*a* and *b*) is also exhibited in the numerical representation (Fig. 12*a* and *b*).

4. Conclusions

A detailed thermo-mechanical deformation study has been undertaken in testing conditions which simulate the FSW of steel in order to generate data not previously available for steel grade DH36 which are expected to improve the accuracy of any predictive modelling work on the subject and contribute towards the fundamental understanding of the process. Analysis of the deformation behaviour of DH36 steel in hot compression tests on a Gleeble 3800 thermo-mechanical testing system has

shown that the evolution of flow stress is significantly affected by the test temperature and the rate of deformation; the alloy's flow stress is seen to increase with increasing strain rate and decreasing temperature. Flow stress in low strain rate-high temperature conditions demonstrates a typical softening phenomenon by DRX. However, the effect of DRX is clearly decreased in high strain rate conditions.

Further, the alloy's flow stress behaviour is only contradicted by the tests at 800^{o}C, where the flow stress is seen to increase compared to that of a lower test temperature for a given strain rate. This atypical behaviour is expected to be a result of the dual phase microstructure of ferrite and austenite which is formed at this inter-critical temperature. This represents an important observation on the optimum conditions for FSW with regards to establishing process parameters and improving tooling and welding machine specifications.

Moreover, the development of a 3D thermo-fluid model, based on a Eulerian formulation and taking into account the plastic deformation and frictional heat generation, has been presented in terms of mechanical equations which govern material flow. The expressed flow stress constitutive equation is established on the Norton Hoff law to predict the behaviour of DH36 steel during FSW. The material deformation constants of this law have been identified using the generated thermo-mechanical deformation data.

The numerical model simulates the material flow and temperature distribution during FSW of steel. Numerical analyses have been performed with the identified material constants; comparison of the welding regions from experimental observations and simulations exhibits very good trends in terms of overall geometry and temperature distribution in the HAZ and TMAZ.

Subsequent work will assess the impact of the thermal cycle and deformation rate by microstructural characterisation and comparison to actual FSW samples.

Acknowledgements

The authors gratefully acknowledge the financial support of the European Union which has funded this work as part of the Collaborative Research Project HILDA (High Integrity Low Distortion Assembly) through the Seventh Framework Programme (SCP2-GA-2012-314534-HILDA).

References

1. W. M. Thomas, P. L. Threadgill and E. D. Nicholas: 'Feasibility of friction stir welding steel', *Sci. Technol. Weld. Join.*, 1999, **4**, 365–372.
2. R. Nandan, T. Debroy and H. K. D. H. Bhadeshia: 'Recent advances in friction-stir welding – Process, weldment structure and properties', *Prog. Mater. Sci.*, 2008, **53**, 980–1023.

3. R. W. Fonda and S. G. Lambrakos: ‘Analysis of friction stir welds using an inverse problem approach’, *Sci. Technol. Weld. Join.*, 2002, **7**, 177–181.
4. X. He, F. Gu and A. Ball: ‘A review of numerical analysis of friction stir welding’, *Prog. Mater. Sci*., 2014, **65**, 1–66.
5. R. S. Mishra and Z. Y. Ma: ‘Friction stir welding and processing’, *Mater. Sci. Eng. R*, 2005, **50**, 1–78.
6. A. P. Reynolds, W. D. Lockwood and T. U. Seidel: ‘Processing-Property Correlation in Friction Stir Welds’, *Mater. Sci. Forum.*, 2000, **331-337**, 1719–1724.
7. P. L. Threadgill, A. J. Leonard, H. R. Shercliff and P. J. Withers: ‘Friction stir welding of aluminium alloys’, *Int. Mater. Rev.*, 2009, **54**, 49–93.
8. T. Lienert, W. Stellwag, B. Grimmett and R. Warke: ‘Friction stir welding studies on mild steel’, *Weld. J. Res. Suppl.*, 2003, 1–9.
9. A. P. Reynolds, W. Tang, M. Posada and J. Deloach: ‘Friction stir welding of DH36 steel’, *Sci. Technol. Weld. Join.*, 2003, **8**, 455–460.
10. N. A. McPherson, A. M. Galloway, S. R. Cater and S. J. Hambling: ‘Friction stir welding of thin DH36 steel plate’, *Sci. Technol. Weld. Join.*, 2013, **18**, 441–450.
11. A. Toumpis, A. Galloway, S. Cater and N. McPherson: ‘Development of a process envelope for friction stir welding of DH36 steel – A step change’, *Mater. Des.*, 2014, **62**, 64–75.
12. A. Nowotnik: ‘Flow stress value and activation energy of hot deformed Inconel superalloys’, *Adv. Manuf. Sci. Technol.*, 2008, **32**, 51–62.
13. P. Boisse, T. Altan and K. van Luttervelt (eds.): ‘Friction and flow stress in forming and cutting’; 2003, London, Kogan Page Science.
14. G. E. Dieter, H. A. Kuhn and S. L. Semiatin (eds.): ‘Handbook of Workability and Process Design’; 2003, Materials Park, OH, ASM International.
15. Y. C. Lin, M.-S. Chen and J. Zhong: ‘Effect of temperature and strain rate on the compressive deformation behavior of 42CrMo steel’, *J. Mater. Process. Technol.*, 2008, **205**, 308–315.
16. M. Zahedul, H. Khandkar and J. A. Khan: ‘Thermal Modeling of Overlap Friction Stir Welding for Al-Alloys’, *J. Mater. Process. Manuf. Sci.*, 2001, **10**, 91–105.
17. A. Simar, J. Lecomte-Beckers, T. Pardoen and B. de Meester: ‘Effect of boundary conditions and heat source distribution on temperature distribution in friction stir welding’, *Sci. Technol. Weld. Join.*, 2006, **11**, 170–177.
18. A. M. Maniatty, Y. Liu, O. Klaas and M. S. Shephard: ‘Stabilized finite element method for viscoplastic flow: formulation and a simple progressive solution strategy’, *Comput. Methods Appl. Mech. Eng.*, 2001, **190**, 4609–4625.

19. S. K. Rajput, M. Dikovits, G. P. Chaudhari, C. Poletti, F. Warchomicka, V. Pancholi and S. K. Nath: 'Physical simulation of hot deformation and microstructural evolution of AISI 1016 steel using processing maps', *Mater. Sci. Eng. A*, 2013, **587**, 291–300.
20. S. M. Abbasi and A. Momeni: 'Hot working behavior of Fe–29Ni–17Co analyzed by mechanical testing and processing map', *Mater. Sci. Eng. A*, 2012, **552**, 330–335.
21. J. Zhang, H. Di, X. Wang, Y. Cao, J. Zhang and T. Ma: 'Constitutive analysis of the hot deformation behavior of Fe–23Mn–2Al–0.2C twinning induced plasticity steel in consideration of strain', *Mater. Des.*, 2013, **44**, 354–364.
22. C. Y. Liu, R. J. Zhang and Y. N. Yan: 'Hot deformation behaviour and constitutive modelling of P92 heat resistant steel', *Mater. Sci. Technol.*, 2011, **27**, 1281–1286.
23. H. Wei, G. Liu, H. Zhao and R. Kang: 'Hot deformation behavior of two C–Mn–Si based and C–Mn–Al based microalloyed high-strength steels: A comparative study', *Mater. Des.*, 2013, **50**, 484–490.
24. H. Mirzadeh, J. M. Cabrera, J. M. Prado and A. Najafizadeh: 'Hot deformation behavior of a medium carbon microalloyed steel', *Mater. Sci. Eng. A*, 2011, **528**, 3876–3882.
25. R. Kaibyshev and I. Kazakulov: 'Deformation behaviour of Fe-3Si steel', *Mater. Sci. Technol.*, 2004, **20**, 221–228.
26. K. Rao, Y. Prasad and E. Hawbolt: 'Hot deformation studies on a low-carbon steel: Part 1 - flow curves and the constitutive relationship', *J. Mater. Process.*, 1996, **56**, 897–907.
27. R. X. Chai, D. H. Xu and C. Guo: 'Prediction of constitutive behaviour of 20CrMnTiH steel under hot deformation conditions', *Mater. Sci. Technol.*, 2012, **28**, 857–863.
28. Z. Zeng, Y. Zhang and S. Jonsson: 'Deformation behaviour of commercially pure titanium during simple hot compression', *Mater. Des.*, 2009, **30**, 3105–3111.
29. L. Gao and A. A. Luo: 'Hot deformation behavior of as-cast Mg–Zn–Mn–Ce alloy in compression', *Mater. Sci. Eng. A*, 2013, **560**, 492–499.
30. Y. Xu, L. Hu and Y. Sun: 'Deformation behaviour and dynamic recrystallization of AZ61 magnesium alloy', *J. Alloys Compd.*, 2013, **580**, 262–269.
31. H. Zhang, N. Jin and J. Chen: 'Hot deformation behavior of Al-Zn-Mg-Cu-Zr aluminum alloys during compression at elevated temperature', *Trans. Nonferrous Met. Soc. China*, 2011, **21**, 437–442.

32. B. Roebuck, J. D. Lord and M. Brooks: ‘Measurement Good Practice Guide No 3. Measuring Flow Stress in Hot Axisymmetric Compression Tests’, National Physical Laboratory, Teddington, Middlesex, UK, 2002

33. A. Bastier, M. H. Maitournam, K. Dang Van and F. Roger: ‘Steady state thermomechanical modelling of friction stir welding’, *Sci. Technol. Weld. Join.*, 2006, **11**, 278–288.

34. R. Nandan, G. G. Roy, T. J. Lienert and T. Debroy: ‘Three-dimensional heat and material flow during friction stir welding of mild steel’, *Acta Mater.*, 2007, **55**, 883–895.

35. X. Zhu and Y. Chao: ‘Numerical simulation of transient temperature and residual stresses in friction stir welding of 304L stainless steel’, *J. Mater. Process. Technol.*, 2004, **146**, 263–272.

36. G. Buffa, J. Hua, R. Shivpuri and L. Fratini: ‘A continuum based fem model for friction stir welding-model development’, *Mater. Sci. Eng. A*, 2006, **419**, 389–396.

37. M. Assidi and L. Fourment: ‘Accurate 3D friction stir welding simulation tool based on friction model calibration’, *Int. J. Mater. Form.*, 2009, **2**, 327–330.

38. H. Schmidt and J. Hattel: ‘Modelling heat flow around tool probe in friction stir welding’, *Sci. Technol. Weld. Join.*, 2005, **10**, 176–186.

39. D. Jacquin, B. de Meester, A. Simar, D. Deloison, F. Montheillet and C. Desrayaud: ‘A simple Eulerian thermomechanical modeling of friction stir welding’, *J. Mater. Process. Technol.*, 2011, **211**, 57–65.

40. P. Ulysse: ‘Three-dimensional modeling of the friction stir-welding process’, *Int. J. Mach. Tools Manuf.*, 2002, **42**, 1549–1557.

41. R. Nandan, G. G. Roy, T. J. Lienert and T. DebRoy: ‘Numerical modelling of 3D plastic flow and heat transfer during friction stir welding of stainless steel’, *Sci. Technol. Weld. Join.*, 2006, **11**, 526–537.

42. M. Chiumenti, M. Cervera, C. Agelet de Saracibar and N. Dialami: ‘Numerical modeling of friction stir welding processes’, *Comput. Methods Appl. Mech. Eng.*, 2013, **254**, 353–369.

43. D. Santiago, G. Lombera, S. Urquiza, A. Cassanelli and L. de Vedia: ‘Numerical modeling of welded joints by the “Friction Stir Welding” process’, *Mater. Res.*, 2004, **7**, 569–574.

44. P. A. Colegrove and H. R. Shercliff: ‘Development of Trivex friction stir welding tool Part 2 – three-dimensional flow modelling’, *Sci. Technol. Weld. Join.*, 2004, **9**, 352–361.

45. P. A. Colegrove and H. R. Shercliff: ‘3-Dimensional CFD modelling of flow round a threaded friction stir welding tool profile’, *J. Mater. Process. Technol.*, 2005, **169**, 320–327.

46. B. C. Liechty and B. W. Webb: ‘Modeling the frictional boundary condition in friction stir welding’, *Int. J. Mach. Tools Manuf.*, 2008, **48**, 1474–1485.

47. M. Assidi, L. Fourment, S. Guerdoux and T. Nelson: ‘Friction model for friction stir welding process simulation: Calibrations from welding experiments’, *Int. J. Mach. Tools Manuf.*, 2010, **50**, 143–155.

48. Z. Zhang: ‘Comparison of two contact models in the simulation of friction stir welding process’, *J. Mater. Sci.*, 2008, **43**, 5867–5877.

Figure captions

Figure 1: Temperature distribution map of a typical FSWeld (Project HILDA)

Figure 2: The Gleeble testing chamber

Figure 3: Flow stress chart for 2 tests at 1100^{o}C–10 s^{-1}

a heating stage; *b* equalising and deformation stage; *c* cooling stage
Figure 4: Temperature profile for the 3 tests at 800^{o}C - 10^{-1} s^{-1}

Figure 5: Strain rate profile for test "Repeat 2" at 700^{o}C - 10^{-3} s^{-1}

Figure 6: Evolution of flow stress with increasing strain rate

Figure 7: Evolution of flow stress with increasing temperature

Figure 8: Material consistency as a function of temperature and strain

Figure 9: Strain rate sensitivity as a function of temperature and strain

Figure 10: Mesh of thermo-fluid model

a 200 rpm–100 mm min^{-1}; *b* 500 rpm–400 mm min^{-1}
Figure 11: Temperature distribution for 5.2 mm tool penetration depth

a 200 rpm–100 mm min^{-1}; *b* 500 rpm–400 mm min^{-1}
Figure 12: TMAZ for 5.2 mm tool penetration depth

a 200 rpm–100 mm min^{-1}; *b* 500 rpm–400 mm min^{-1}
Figure 13: Macrograph of FSWeld of DH36 steel

Table captions

Table 1 Number of tests performed per set of test temperature and strain rate

Table 2 Average flow stress (in MPa) for each set of parameters at 0.3 strain

Figure 1
Click here to download high resolution image

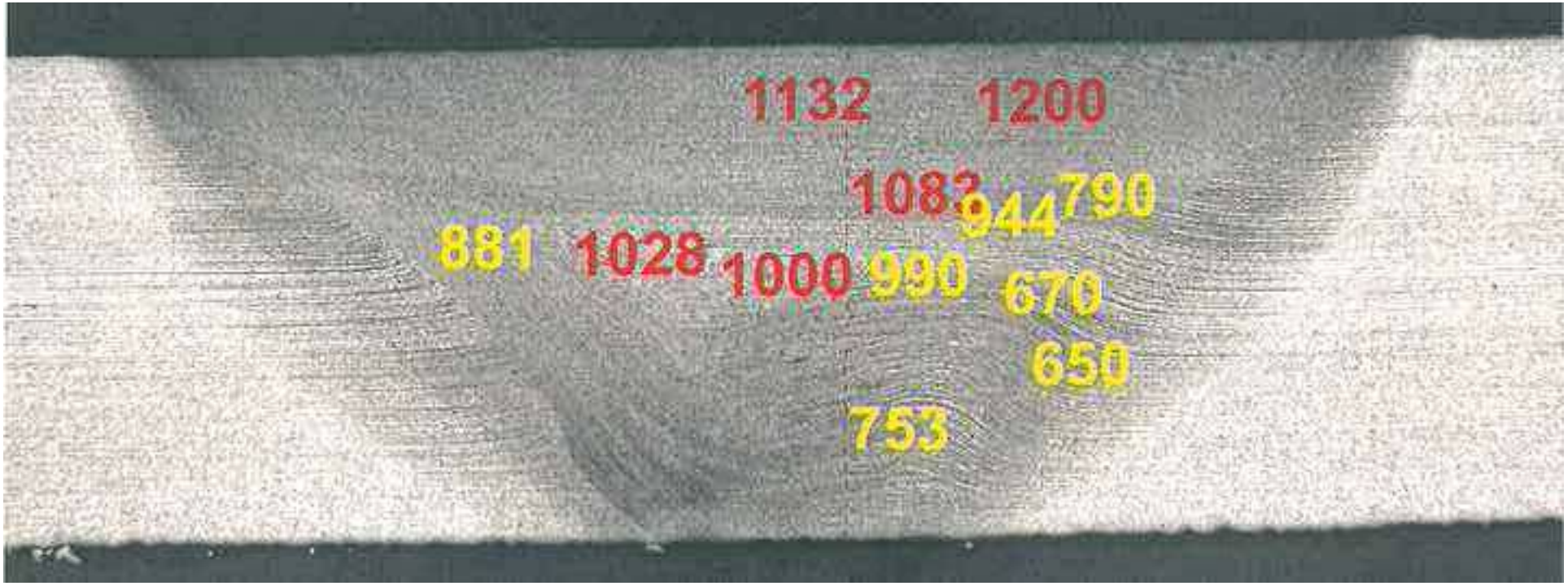

Figure 2
Click here to download high resolution image

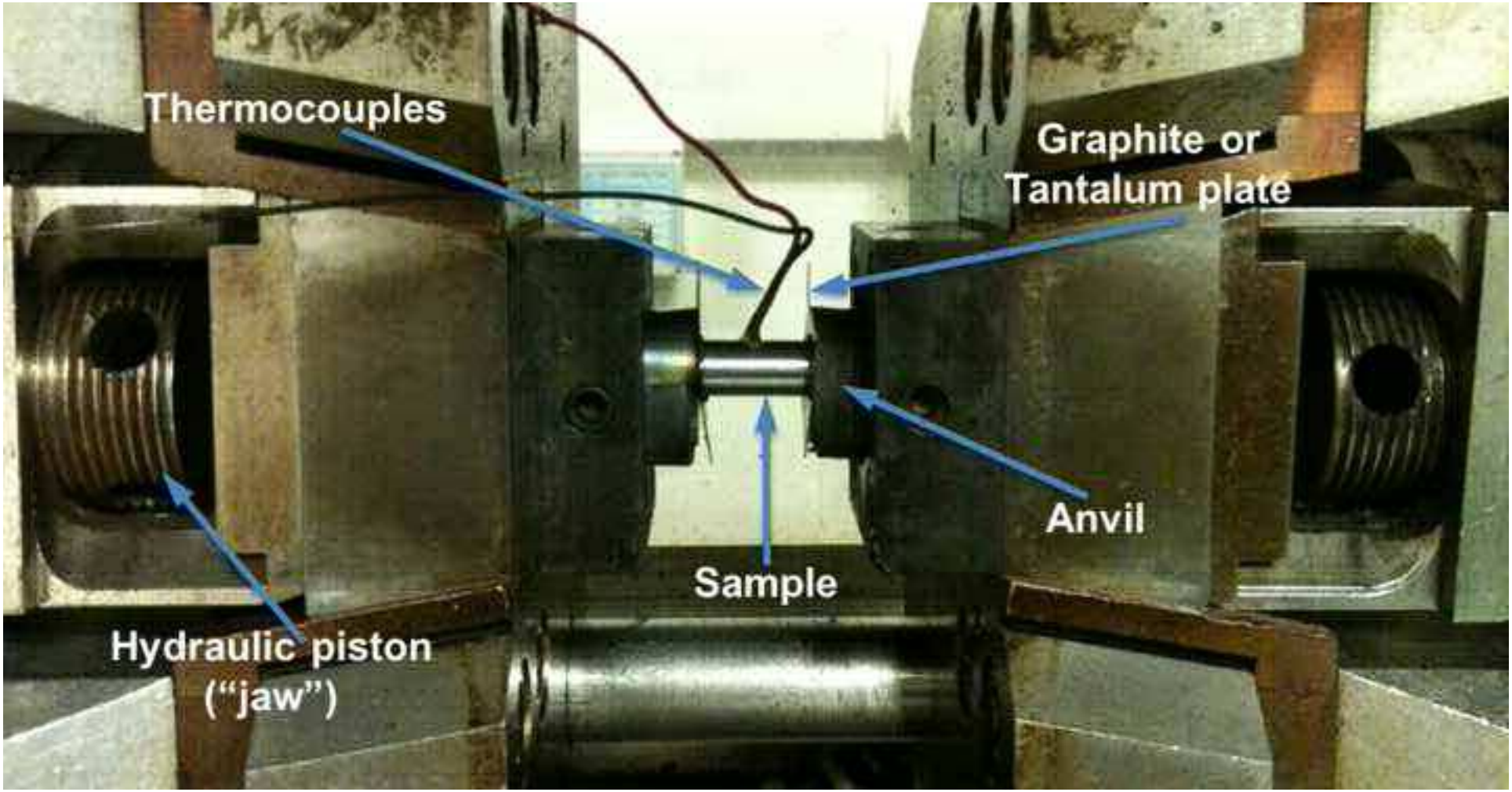

Figure 3
Click here to download Colour figure: Figure 3.xlsx

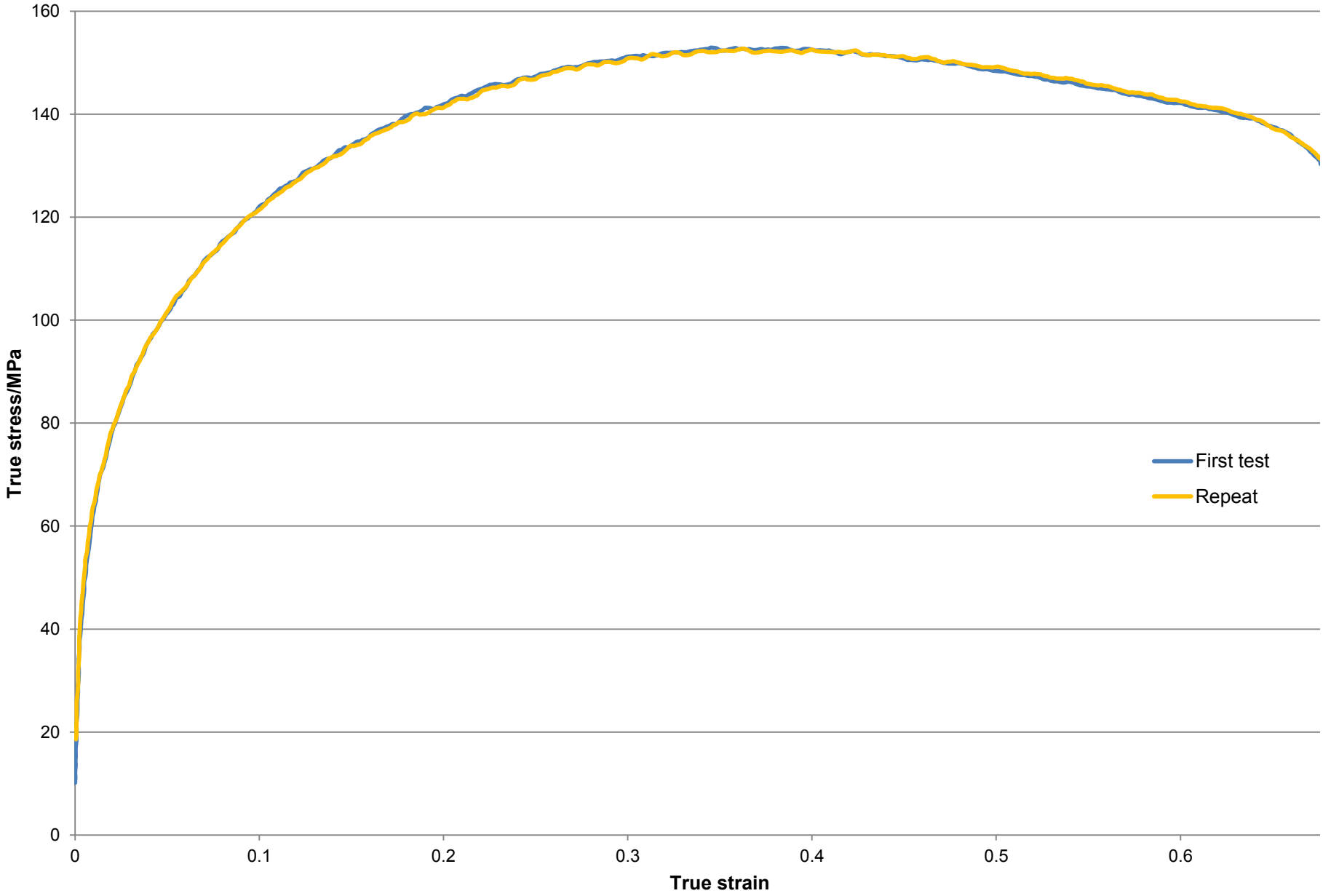

Figure 4
Click here to download Colour figure: Figure 4.xlsx

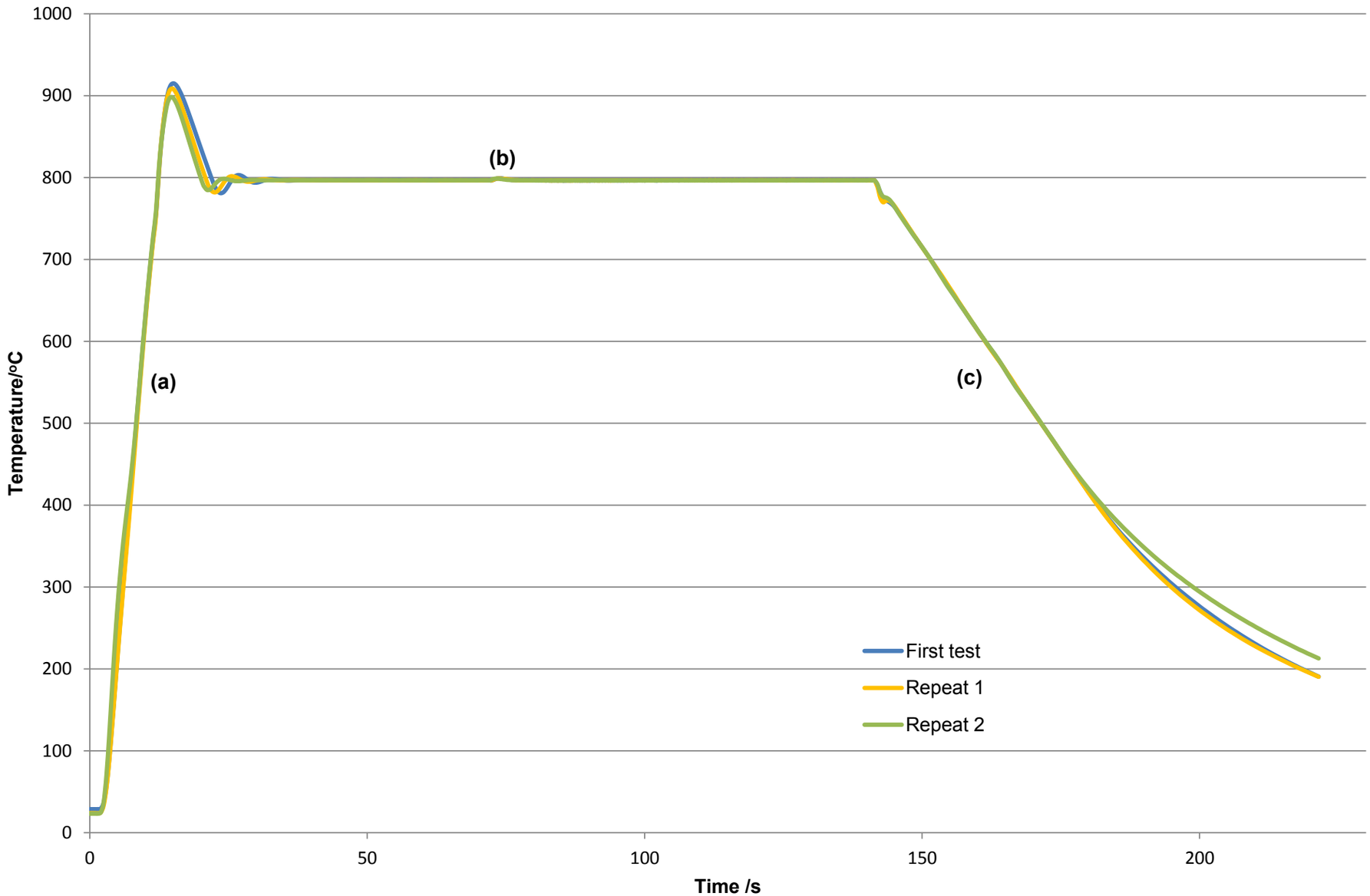

Figure 5
Click here to download Colour figure: Figure 5.xlsx

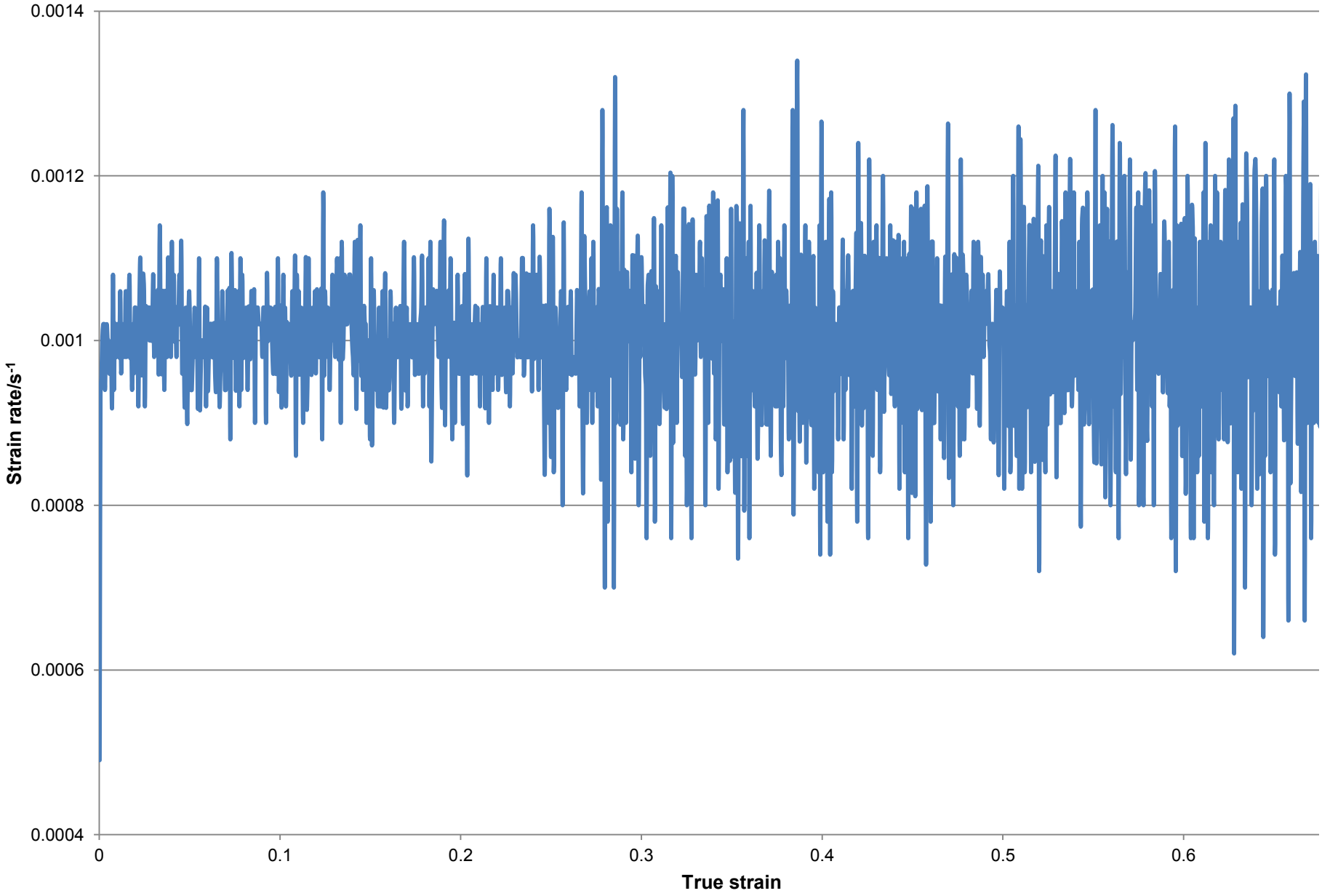

Figure 6
Click here to download Colour figure: Figure 6.xlsx

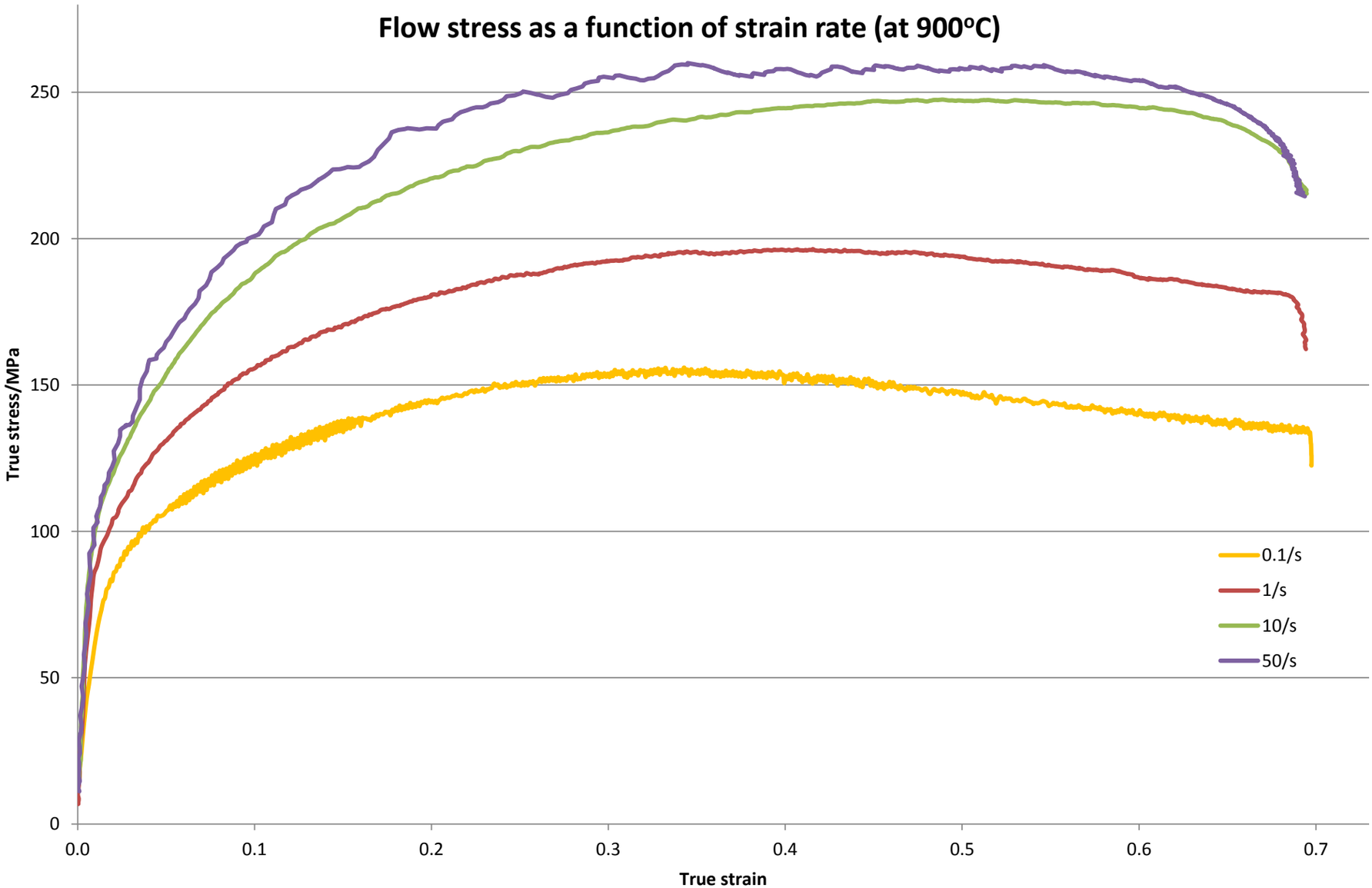

Figure 7
Click here to download Colour figure: Figure 7.xlsx

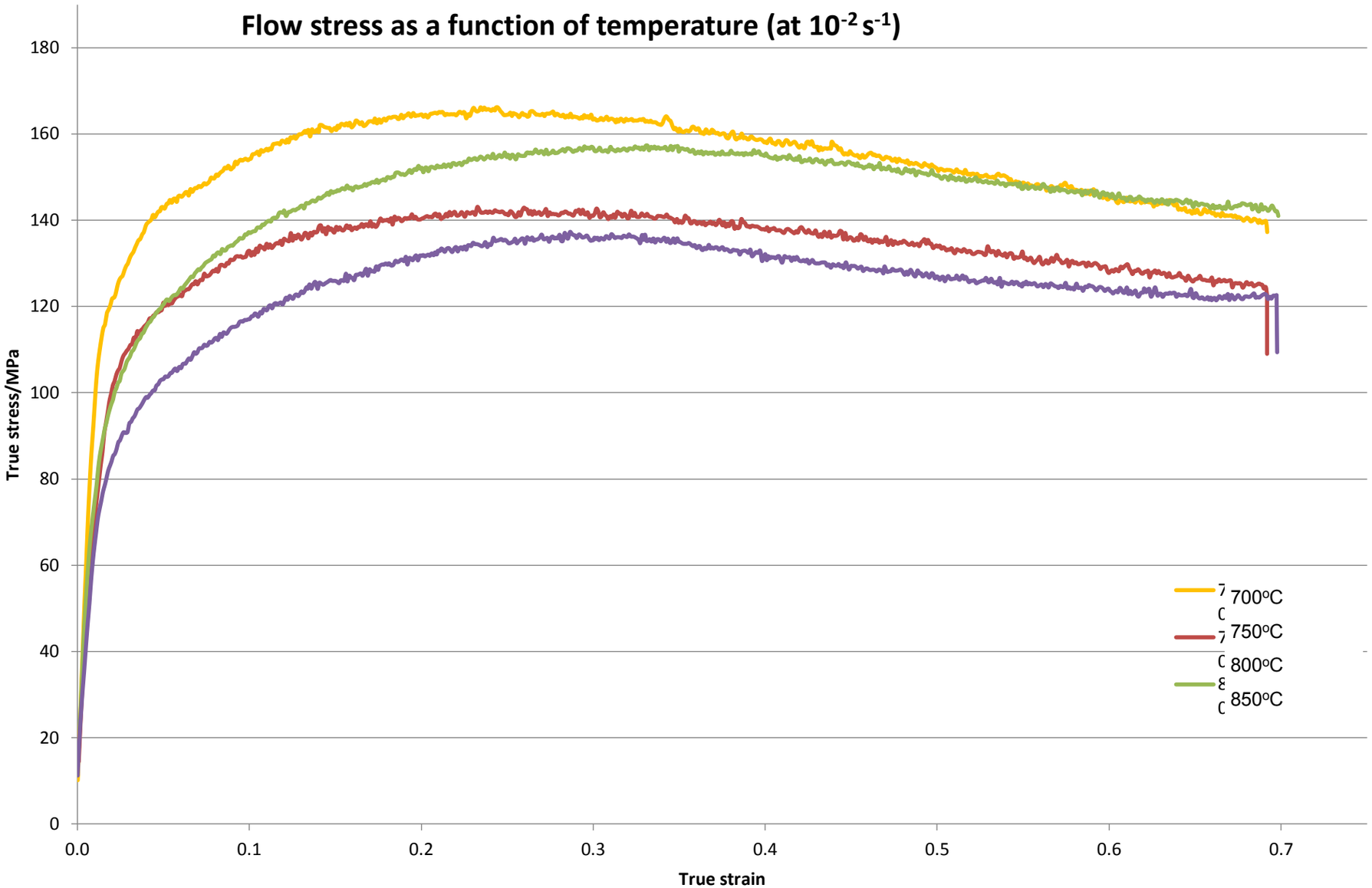

Figure 8
Click here to download Colour figure: Figure 8.xlsx

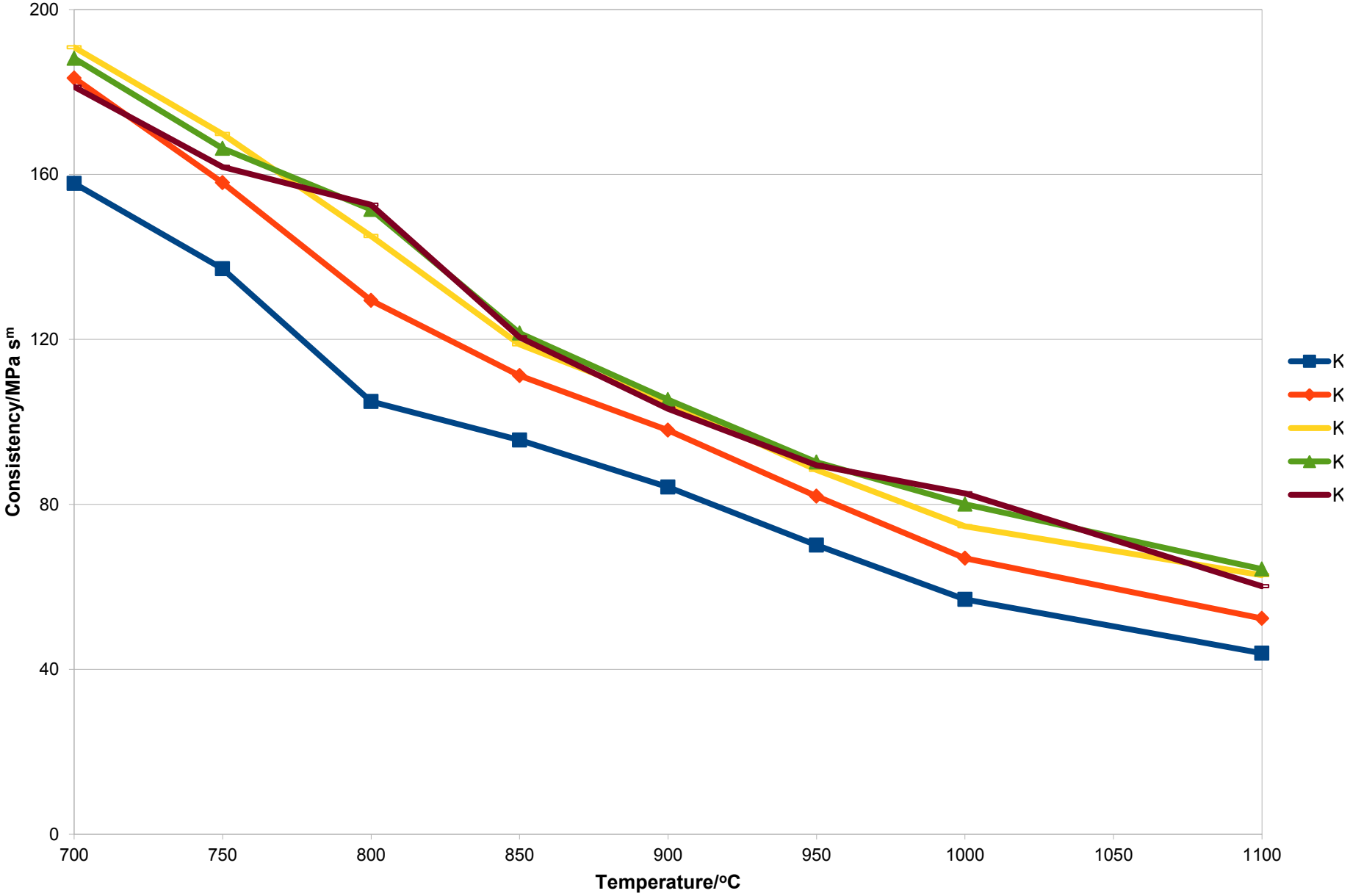

Figure 9
Click here to download Colour figure: Figure 9.xlsx

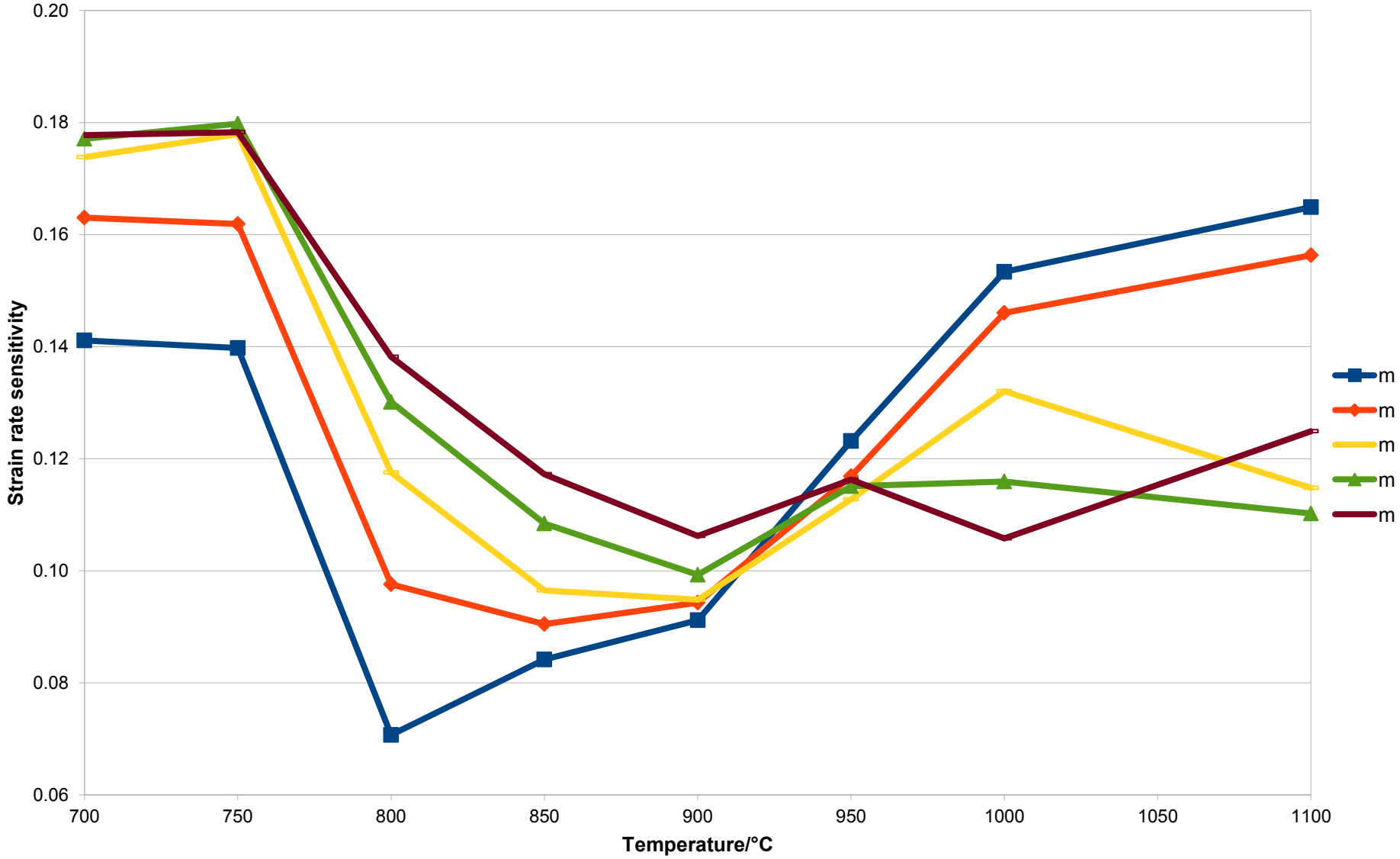

Figure 10
Click here to download high resolution image

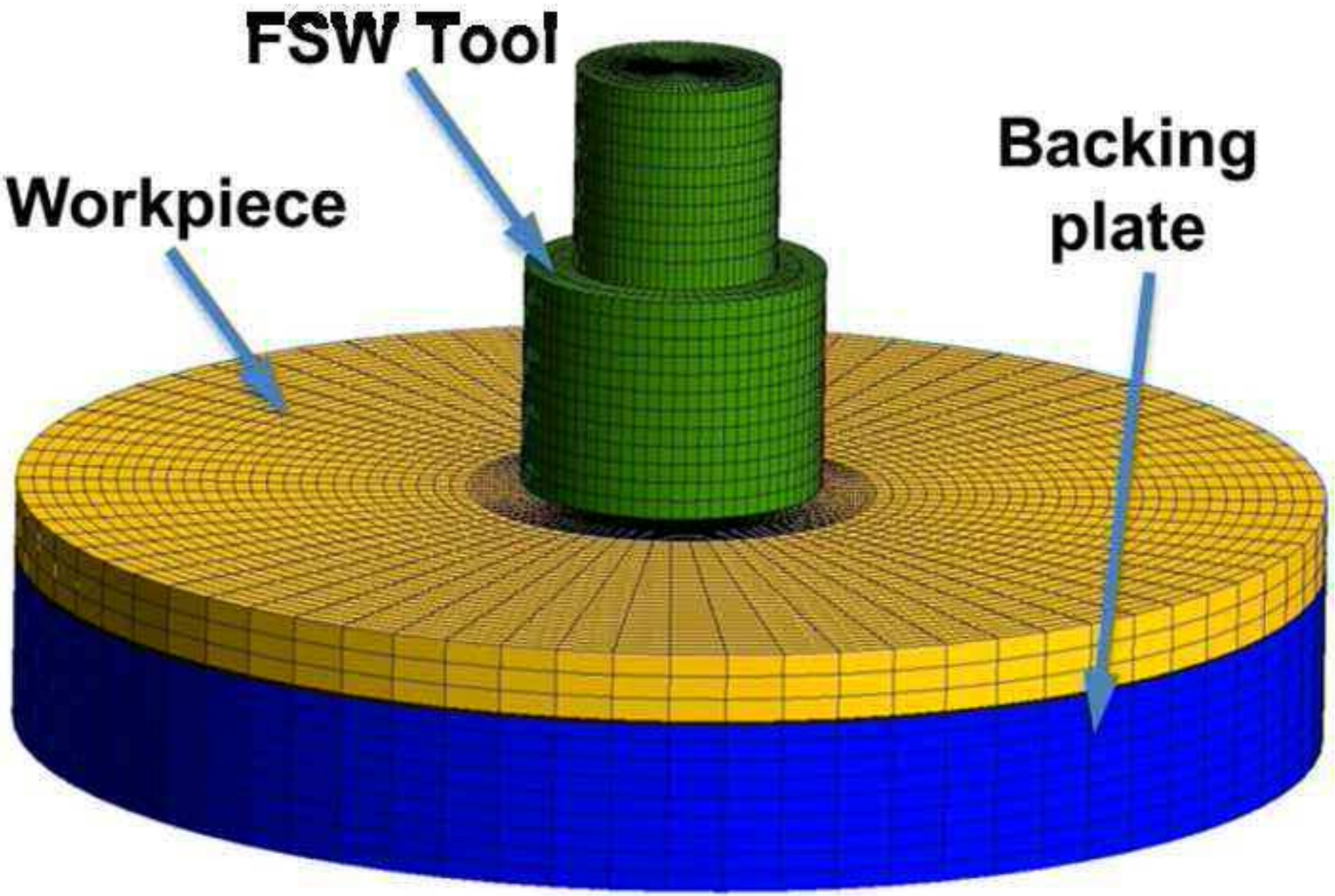

Figure 11 (a)
Click here to download high resolution image

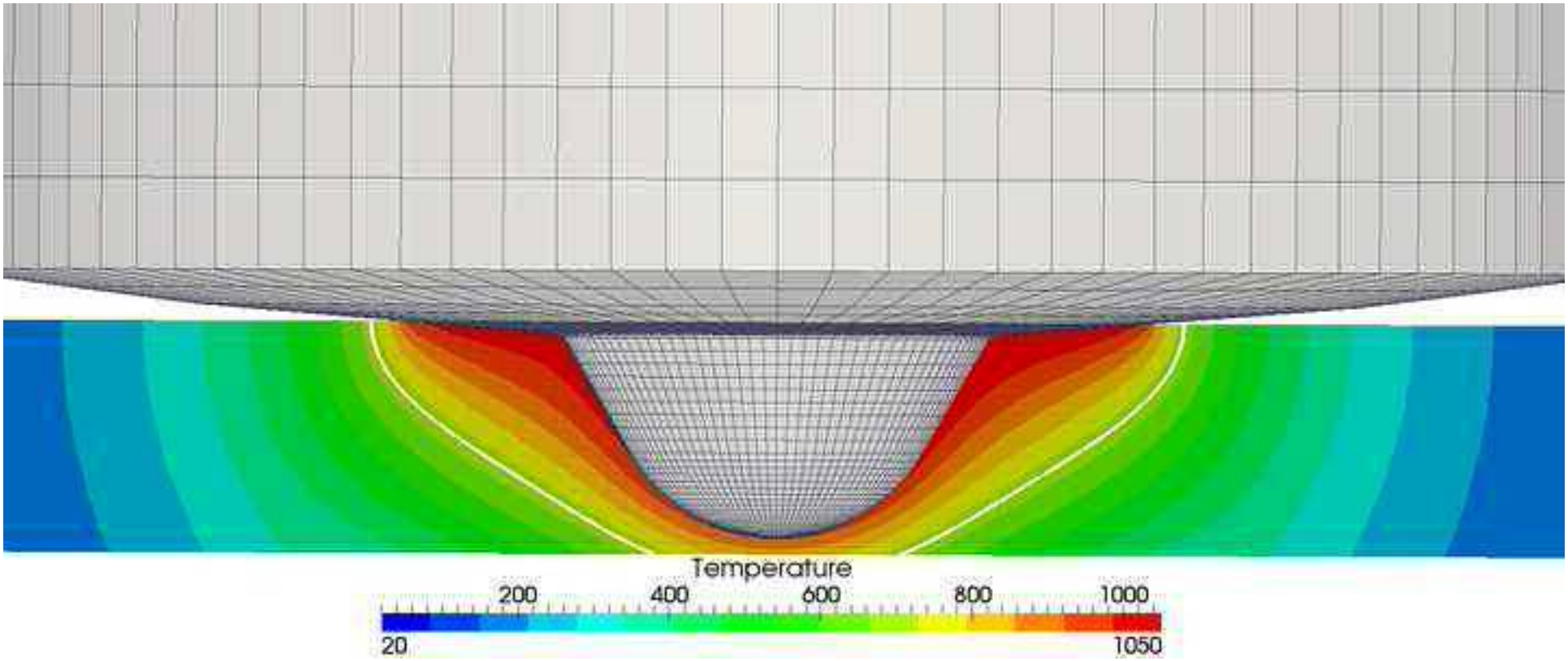

Figure 11 (b)
Click here to download high resolution image

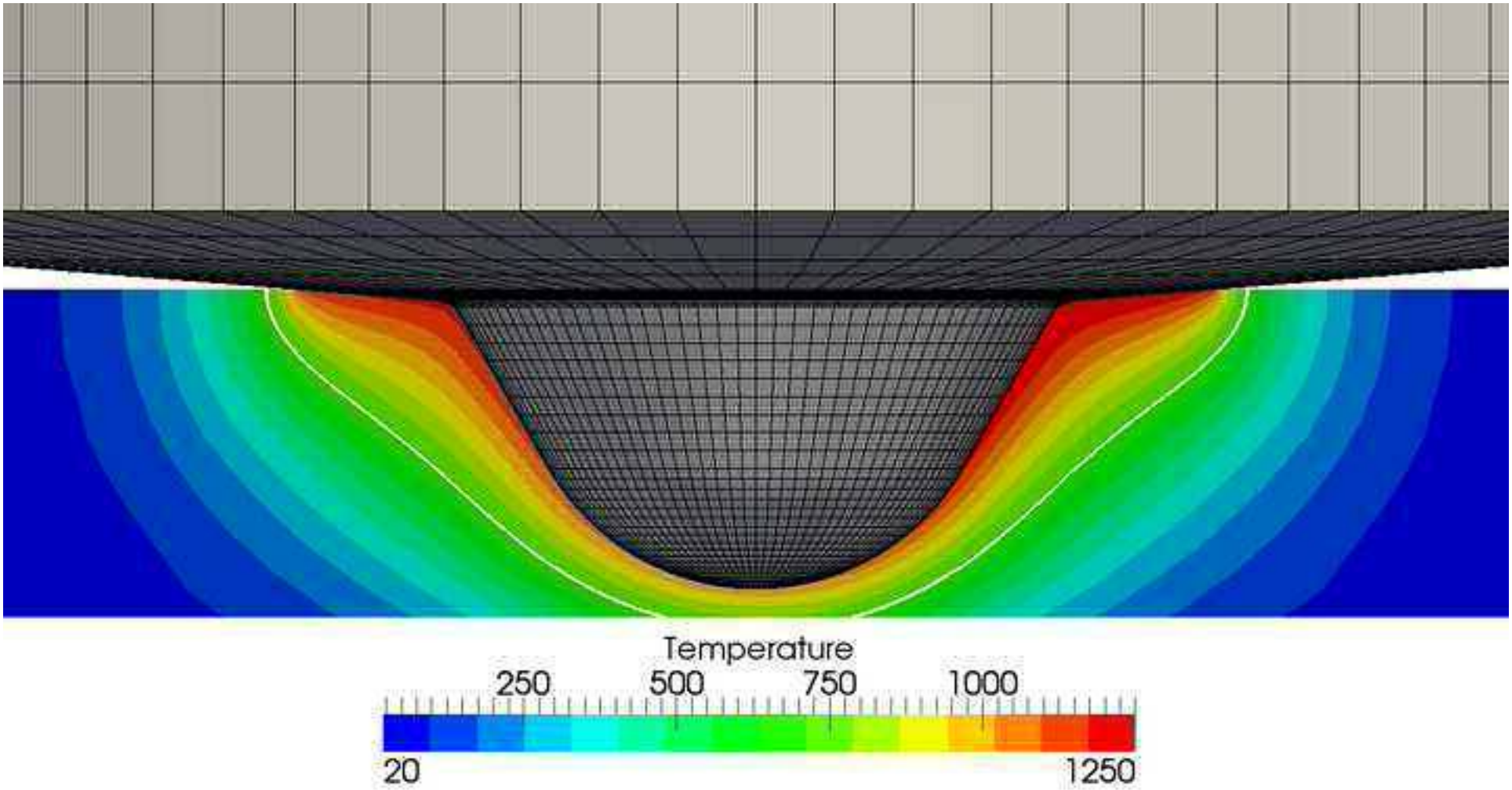

Figure 12 (a)
Click here to download high resolution image

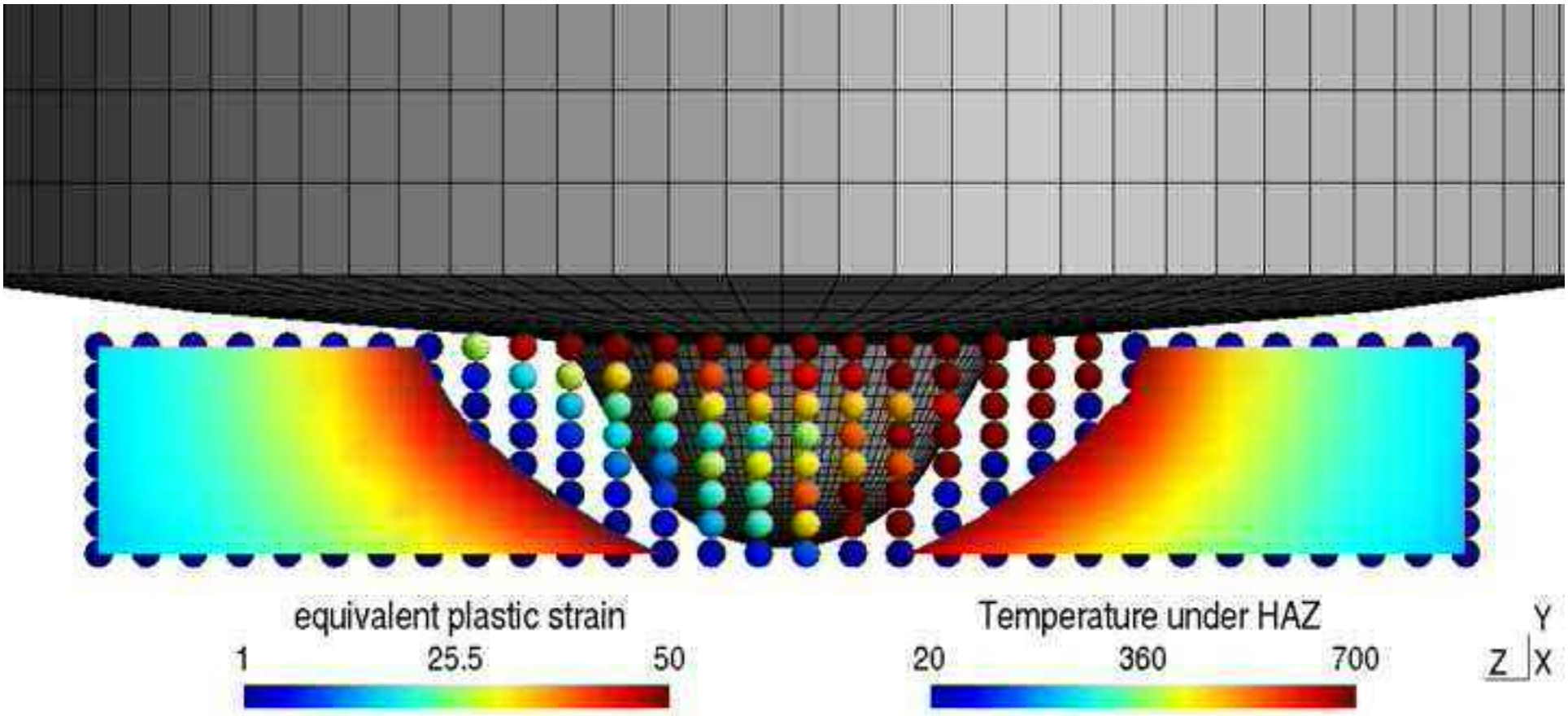

Figure 12 (b)
Click here to download high resolution image

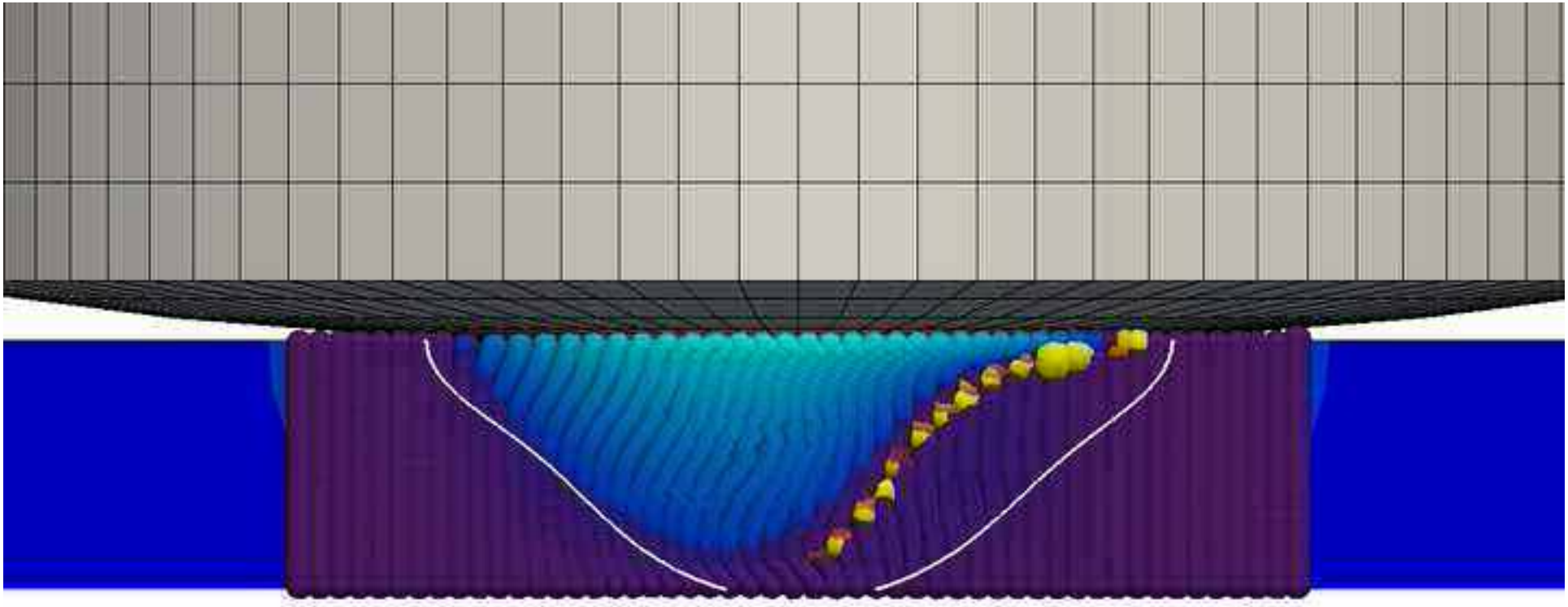

Figure 13 (a)
Click here to download high resolution image

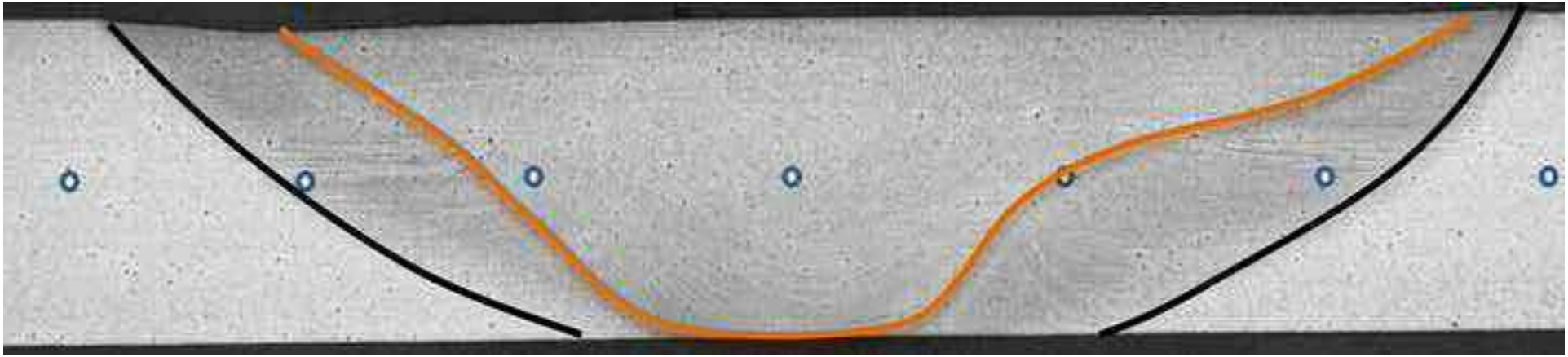

Figure 13 (b)
Click here to download high resolution image